Efficient Adsorption-Assisted Photocatalysis Degradation of Congo Red through Loading ZIF-8 on KI-Doped TiO$_2$

Zhechen Liu [1,†], Wanqi Zhang [1,†], Xilong Zhao [1,†], Xianliang Sheng [2], Zichu Hu [2], Qiang Wang [2], Zhangjing Chen [3], Sunguo Wang [4], Xiaotao Zhang [2,5,*] and Ximing Wang [1,5,*]

[1] College of Material Science and Art Design, Inner Mongolia Agricultural University, Hohhot 010018, China; liuzhechen@emails.imau.edu.cn (Z.L.); nmgndcyyzwq@emails.imau.edu.cn (W.Z.); xilonghappy@163.com (X.Z.)

[2] College of Science, Inner Mongolia Agricultural University, Hohhot 010018, China; shengxl@iccas.ac.cn (X.S.); huzichu@emails.imau.edu.cn (Z.H.); 2019122144691@emails.imau.edu.cn (Q.W.)

[3] Department of Sustainable Biomaterials, Virginia Polytechnic Institute and State University, Blacksburg, VA 24060, USA; chengo@vt.edu

[4] Sungro Bioresource & Bioenergy Technologies Corporation, Edmonton, AB T6R 3J6, Canada; wangsunguo@gmail.com

[5] Inner Mongolia Key Laboratory of Sandy Shrubs Fibrosis and Energy Development and Utilization, Hohhot 010018, China

[*] Correspondence: lianzixiaotao@163.com (X.Z.); wangximing@imau.edu.cn (X.W.)

[†] These authors contributed equally to this work.

Abstract: Zeolitic imidazolate framework-8 (ZIF-8) was evenly loaded on the surface of TiO$_2$ doped with KI, using a solvent synthesis method, in order to produce a ZIF-8@TiO$_2$ (KI) adsorption photocatalyst with good adsorption and photocatalytic properties. The samples were characterized by XRD, SEM, EDX, XPS, BET and UV-Vis. The photocatalytic efficiency of the material was obtained by photocatalytic tests. The results indicate that the doping with I inhibited the grain growth and reduced the crystallite size of TiO$_2$, reduced the band gap width and improved the utilization rate for light. TiO$_2$ (KI) was a single crystal of anatase titanium dioxide. The combination of ZIF-8 and TiO$_2$ (KI) improved the specific surface area and increased the reaction site. The ZIF-8@TiO$_2$ (KI) for Congo red was investigated to validate its photocatalytic performance. The optimal concentration of Congo red solution was 30 mg/L, and the amount of catalyst was proportional to the degradation efficiency. The degradation efficiency of ZIF-8@TiO$_2$ (5%KI) was 76.42%, after being recycled four times.

Keywords: ZIF-8; TiO$_2$ (KI); photocatalysis; Congo red

1. Introduction

Dye wastewater mainly comes from the textile, dyeing, paper, leather, coating and dye manufacturing industries [1]. The scale of China's textile production is the largest in the world, as a major player in the textile industry. A total of 10–15% of dyes escape and enter the water, which is treated and then discharged in the process of textile printing and dyeing [2,3]. Only 1 t of dye of can pollute 20 t of water, and so the degree of pollution and damage caused by dye to water is very large [4]. Long-term contact will damage human organs and lead to nervous system disorders. Most azo dyes can lead to cell mutations, gene mutations and body deformations [5]. The most widely used azo dyes have been proved to cause bladder cancer, spleen tumors and liver cancer [6]. The anionic dye Congo red is widely used in the textile industry and is difficult to be degraded [7,8]. Dye degradation methods include physical, chemical and biological methods [9]. Congo red dye can be degraded by adsorption, as a physical method, and photocatalysis, as a chemical method.

TiO$_2$ shows excellent photocatalytic performance and has been widely studied for its good chemical stability, low cost, diverse preparation methods, low harm and high catalytic efficiency [10]. The degradation efficiency of TiO$_2$ under UV light is low, and so it

requires modification to improve its catalytic performance. Non-metallic N doping in TiO_2 shows good performance [11]. Previous studies showed that the catalytic performance of halogen-I-doped TiO_2 is higher than that of N [12]. Iodine has a variety of oxidation states, and the surface charge of the catalyst is easy to change. The doping of iodine can produce more oxygen vacancies, reduce the band gap width and improve the utilization rate of ultraviolet light [13].

MOFs have adjustable channels, a large specific surface area, good stability and unsaturated metal sites [14]. The zeolitic imidazolate framework-8 (ZIF-8) in MOFs is composed of Zn^{2+} or Co^{2+}, complexed with N atoms on imidazole ligands to form zeolite-like coordination polymers [15]. ZIF-8 has high thermal and chemical stability, and can maintain its complete structure at high temperature; the porosity of the material also does not change. MOFs@TiO_2 has a synergistic effect to improve photocatalytic performance by accelerating the transfer of photogenerated electrons [16]. ZIF-8 increases the specific surface area of TiO_2, which provides a large number of reaction sites for TiO_2 and inhibits the recombination of electrons and holes.

Although ZIF-8@TiO_2 has been the focus of many scholars [17–21], ZIF-8@TiO_2 (KI) has not yet been studied. ZIF-8, KI and TiO_2 were combined for the first time to degrade Congo red under UV irradiation. We prepared ZIF-8@TiO_2 (5%KI) for the first time. The degradation performance of Congo red is superior to that of other photocatalytic materials. In this paper, the united technologies of adsorption and photocatalysis were used to catalyze Congo red solution in organic dyes. ZIF-8 material in MOFs with a large specific surface area and strong stability was used as the adsorption material, and TiO_2 was used as the photocatalytic material. ZIF-8 solved the problems of the small specific surface area and insufficient reaction sites of TiO_2. Doping TiO_2 with I improved the photocatalytic degradation efficiency of TiO_2.

2. Materials and Methods

2.1. Materials

Potassium iodide, 2-methylimidazole and tetrabutyl titanate were purchased from Macklin (Shanghai, China); N, N-dimethylformamide (DMF), anhydrous ethanol, polyethylene glycol 400 (PEG-400) and Congo red were purchased from Fuchen Chemical (Tianjin, China); glacial acetic acid was purchased from Kemao Chemical (Tianjin, China), and zinc nitrate hexahydrate was purchased from Aike Chemical (Chengdu, China).

2.2. Preparation and Testing of Photocatalyst

2.2.1. Preparation of TiO_2 (KI)

Liquid A: 5 mL glacial acetic acid, 2.5 mL deionized water, 1 mL PEG-400 and potassium iodide (KI) were added to 10 mL absolute ethanol and stirred well. Liquid B: 10 mL tetrabutyl titanate was slowly added to 15 mL absolute ethanol and stirred evenly. Liquid A and liquid B were then stirred vigorously in a magnetic stirrer for 20–30 min at room temperature. Liquid A was slowly dropped into liquid B, which was then stirred vigorously for 2 h after liquid A and liquid B were stirred separately. When the amount of KI increased, the color changed from milky white to light yellow. The sol was sealed in a beaker and stored in a dark place for 24 h to form a soft elastic white solid gel, which was placed in a vacuum drying oven and dried at 100 °C for 24 h to form granular crystals of xerogel. The xerogel was ground into powder in a mortar. The solid particles were ground into a white (low KI) or light yellow (high KI) powder. The finished powder was placed in the crucible, which was placed in a box-type furnace for calcination. The temperature was selected as 350 °C for heating and calcining. The powder in the lower layer was processed through a 200-mesh sieve and then used for the photocatalytic experiment after calcination. The treated TiO_2 was recorded as TiO_2 (350 °C).

2.2.2. Preparation of ZIF-8@TiO$_2$ (5%KI)

In total, 477.8 mg Zn(NO$_3$)$_2$6H$_2$O, 120 mg 2-methyl imidazole and 0.2 g TiO$_2$ (5%KI) were added to 36 mL DMF. The samples were ultrasonicated for 20 min at room temperature. The samples after ultrasound were placed in a 100 mL stainless steel autoclave which was placed in an electric drying oven. The temperature was raised to 140 °C at 5 °C/min and then thermally insulated for 24 h. The temperature was reduced to room temperature at a rate of 0.4 °C/min. The yellow crystalline solids were removed from the inner tank of the stainless-steel autoclave, which was washed with DMF and centrifuged three times, before being dried in a vacuum drying oven at 60 °C for 5 h and ground into powder. For convenience of description, the composite material is represented as ZIF-8@TiO$_2$ (5%KI).

2.2.3. Evaluation of Photocatalytic Activity

A catalyst of a certain weight was added to 100 mL Congo red solution, which was placed in a photocatalytic reaction tube. After 30 min of reaction in a dark environment, the adsorption equilibrium between the sample and Congo red solution was achieved, and the influence of adsorption on the photocatalytic effect was avoided [22,23]. After reaction in the dark for 30 min, the mercury lamp was turned on, and 5 mL of the reaction Congo red solution was added to the centrifuge tube every 20 min and centrifuged at a speed of 8000 rpm. The supernatant was taken for a wavelength test at 497 nm. As shown in Figure S1 (in the Supplementary Materials), the maximum absorption wavelength is 497 nm [24]. The photocatalytic efficiency was calculated according to Equation (1).

$$\eta = 1 - A_t/A_0 \tag{1}$$

where η is the photocatalytic efficiency, A_0 is the initial absorbance value of the sample and A_t is the absorbance value of the solution after photocatalytic time t.

The kinetics of the photodegradation was modeled using the first-order kinetics:

$$ln(A_0/A_t) = ln(C_0/C_t) = k_1t \tag{2}$$

where A_0 is the initial absorbance value of the sample, A_t is the absorbance value of the solution after photocatalytic time t, k_1 (min^{-1}) is photodegradation rate constant and t (min) is the photocatalytic time.

2.3. Characterization

The crystal morphology and distribution of ZIF-8@TiO$_2$ (5%KI) was observed with the FEI 650 scanning electron microscope (FEI Company). The element distribution of ZIF-8@TiO$_2$ (5%KI) was observed by EDX test. The morphologies and structures of ZIF-8@TiO$_2$ (5%KI) were analyzed by TEM (JEM-2100F, Tokyo, Japan). We used the X-ray photoelectron spectrometer (AXIS-ULTRA DLD, Kratos Company, UK) to analyze the changes in the valence states of the elements. The specific surface area and pore size were analyzed using a V-Sorb 2800TP (Jinepu Technology, Beijing, China). An X-ray diffractometer (XRD-700S) was used to analyze the crystal type of TiO$_2$ (KI), ZIF-8 and ZIF-8@TiO$_2$ (5%KI). The X-ray source was the Cu target, Kα = 0.15418 nm, the tube voltage was 40 kV, the tube current was 100 mA, the diffraction angle was 2θ and the scanning speed was 10°/min. The crystallite size was calculated and analyzed according to Equation (3) [25].

$$D = K\lambda/(\beta cos\theta) \tag{3}$$

where K is the Scherrer constant of the diffraction peak (0.89), D is the average crystallite size, λ is the wavelength of the X-ray incident wave, valued at 0.15418 nm, β is the half-peak width of the XRD diffraction peak and θ is the Bragg diffraction angle.

The spectra of different powder samples were measured and characterized by Ultraviolet Diffuse Reflectance Spectroscopy (DRS), which used a Tu-1950 dual-beam UV-Vis

spectrophotometer with a scanning range of 200–800 nm. The band gap width was calculated according to Equation (4) [26].

$$(\alpha h\nu)^2 = k(h\nu - Eg) \tag{4}$$

where α is the absorption coefficient, h is Planck's constant, ν is the frequency of the light wave, k is the proportionality constant and Eg is the photon energy (band gap width)

3. Results

3.1. Crystal Structure Analysis of Photocatalyst

Figure 1a shows the XRD diagram of potassium-iodide-doped TiO_2 with different molar ratios and undoped TiO_2. The calcination temperature of all samples was 350 °C and the calcination time was 5 h. The diffraction angles corresponding to the diffraction peaks in Figure 1 were compared with the standard diffraction card (JCPDS No.21-1272). It was found that the sample was calcined at 350 °C for 5 h to produce a single crystal of anatase-type TiO_2. There was no rutile-type or plate-type TiO_2 in the sample. The diffraction angles (2θ) of 25.21°, 37.82°, 47.9° and 62.56° belonged to the crystal planes of (101), (004), (200) and (204) of the anatase type, respectively [27]. It was determined that the prepared TiO_2 was a single anatase-type TiO_2 crystal. As shown in Figure 1a, with the increase in KI content, the diffraction peak of 25.21° became wider and less sharp. Doping with I ions led to the lattice distortion of TiO_2, which weakened the lattice signal and reduced the intensity of the diffraction peak. The XRD test did not detect the related diffraction peak of the iodine compound, indicating that I ions were highly dispersed in TiO_2.
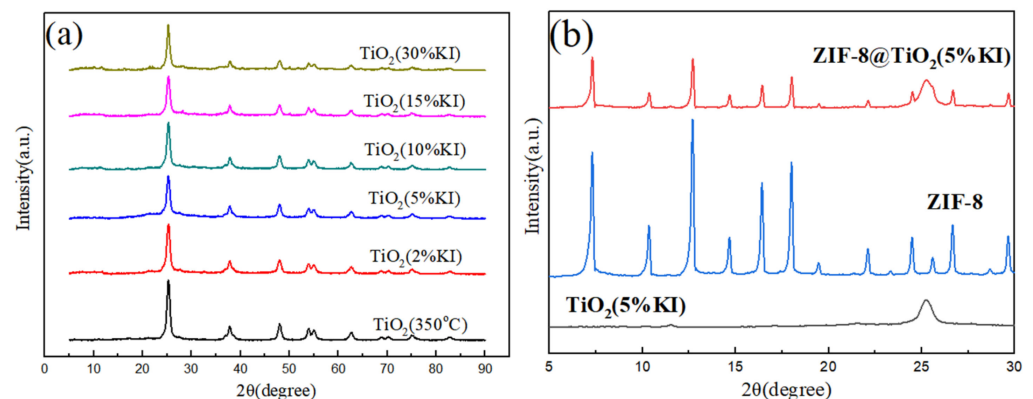

Figure 1. (**a**) XRD patterns of TiO_2 doped with different amounts of I, (**b**) XRD patterns of TiO_2 (5%KI), ZIF-8, ZIF-8@TiO_2 (5%KI).

Figure 1b shows the composite material comparison diagram. It can be seen that the XRD pattern of ZIF-8 presents strong diffraction peaks at 7.35°, 10.34°, 12.68°, 14.66°, 16.5° and 18.0°, corresponding to the crystal planes of (011), (002), (112), (022), (013) and (222), respectively. The position of the diffraction peak was consistent with the standard diffraction card [28]. The crystal plane corresponding to the TiO_2 (5%KI) diffraction angle (2θ) of 25.21° was an anatase-type (101) crystal plane, as shown in Figure 1b. Due to the different intensities of the ZIF-8@TiO_2 (5%KI) peaks, individual diffraction peaks are masked.

The crystallite size can be calculated according to Equation (3). As can be seen from Table 1, after the addition of KI to TiO_2, the crystallite size decreased, which was consistent with the change in XRD peaks.

Table 1. Effect of doping with I on the crystallite size of TiO_2.

Sample	Half Band Width (β)	Bragg Diffraction Angle (2θ)	Bragg Smi-Diffraction Angle (θ)	Crystallite Size (nm)
TiO_2 (350 °C)	0.8096	25.27	12.635	16.99
TiO_2 (2%KI)	0.8758	25.24	12.62	15.69
TiO_2 (5%KI)	0.9433	25.26	12.63	14.58
TiO_2 (10%KI)	0.8431	25.26	12.63	16.31
TiO_2 (15%KI)	0.8508	25.27	12.635	16.17
TiO_2 (30%KI)	0.8386	25.24	12.62	16.39

3.2. Morphology Analysis

Figure 2a shows the SEM image of ZIF-8. Figure 2b–d show the SEM images of ZIF-8@TiO_2 (5%KI). Figure 2e,f show the TEM images of ZIF-8@TiO_2 (5%KI). Figure 2a shows that ZIF-8 was a decahedral sodalite crystal with multiple quadrilateral surfaces [29]. It can be seen from Figure 2b that the material of ZIF-8@TiO_2 (5%KI) was distributed in a lamellar or block shape. With the increase in the number of SEM tests, the fine distribution of micro-spherical TiO_2 (5%KI) can be observed in Figure 2c,d. In these images, the bright part is the micro-spherical TiO_2 (5%KI), and the black part is the block ZIF-8 material under the TiO_2 (5%KI). The agglomeration of TiO_2 (5%KI), which was densely distributed around ZIF-8, is shown in Figure 2d. Figure 2e demonstrates the compound situation of ZIF-8@TiO_2 (5%KI). It can be seen that ZIF-8-coated micro-spherical TiO_2 (5%KI) had a good coating effect. ZIF-8 was on the outside of the composite, and TiO_2 (5%KI) was on the inside of the composite. In Figure 2e, the black spherical part in the middle is the encapsulated and agglomerated TiO_2 (5%KI). Figure 2f provides a magnified view of the agglomeration part of TiO_2 (5%KI). The agglomeration phenomenon was caused by the uneven distribution of TiO_2 (5%KI) in the process of preparing ZIF-8@TiO_2 (5%KI).
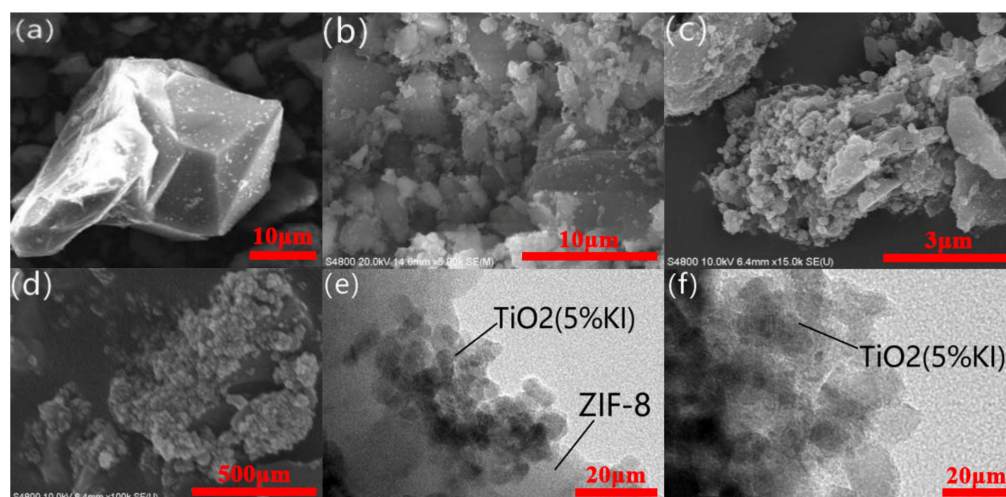
Figure 2. SEM (**a**) of ZIF-8; SEM (**b**–**d**) and TEM (**e**,**f**) of ZIF-8@TiO_2 (5%KI).

3.3. Element Analysis

Figure 3a,b show the EDX images of ZIF-8@TiO_2 (5%KI). Figure 3c is the mapping of a single element. The bond between Ti and O was verified by XRD detection. The distribution of I was the same as that of Ti, which indicates that I was doped into TiO_2 or distributed on the surface of TiO_2. In XRD detection, the doping of TiO_2 with I led to the change in crystallite size, so I was doped into TiO_2 [30]. The distribution of Ti and Zn in the composite material was different, because the distribution of TiO_2 (5%KI) in the composite material was not uniform. TiO_2 (5%KI) exhibited the agglomeration phenomenon and some ZIF-8 did not cover TiO_2 (5%KI). However, the distribution of Ti and Zn was similar at the locations of ZIF-8-coated TiO_2 (5%KI).
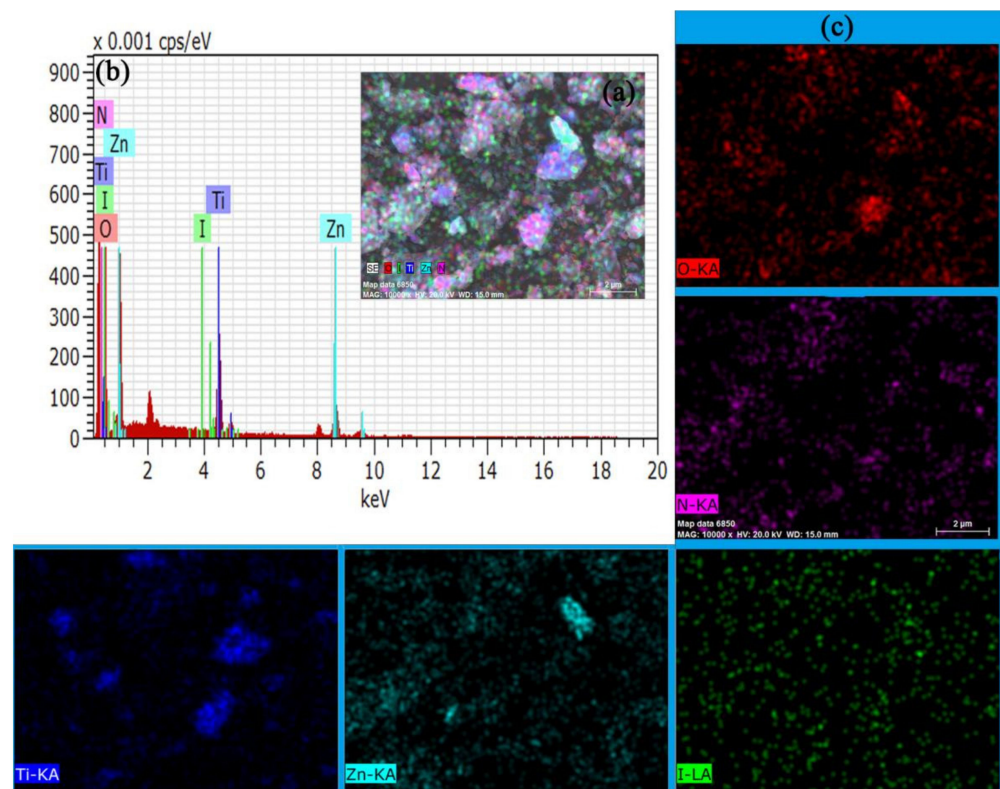
Figure 3. (**a**,**b**) ZIF-8@TiO$_2$ (5%KI) EDX diagram, (**c**) single element EDX diagram of ZIF-8@TiO$_2$ (5%KI).

Figure 4a gives the general diagram of the ZIF-8@TiO$_2$ (5%KI) XPS analysis. Nitrogen, oxygen, titanium, zinc, iodine and other elements were present in the composite material. Figure 4b gives the XPS diagram of N in the composite material. N was present in ZIF-8. Three peaks of N appeared in peak fitting, at 398.7 eV, 399.5 eV and 400.5 eV, which correspond to the pyridine-type nitrogen, pyrrole-type nitrogen and graphite-type nitrogen, respectively [31]. Pyridine-type nitrogen and pyrrole-type nitrogen can improve the adsorption performance of ZIF-8 [32,33]. Graphite-type nitrogen can improve the conductivity of ZIF-8. Figure 4c gives the XPS diagram of oxygen. The molecular formula of ZIF-8 is C$_8$H$_{10}$N$_4$Zn; it was believed that the oxygen present came from the oxygen atom in TiO$_2$. The diffraction peaks of oxygen at 529.47 eV and 531.26 eV correspond to lattice oxygen (529.5 eV) and surface-adsorbed oxygen (531.7 eV), respectively [34]. Because of the doping of I, the diffraction peaks of oxygen shifted. The lattice oxygen came from the oxygen in TiO$_2$ (Ti-O). It can be inferred that Ti-O-I or oxygen holes are generated [35]. The formation mechanism of oxygen holes means that I^{5+} doped with TiO$_2$ generates I$_2$O$_5$, and the surrounding O and I$_2$O$_5$ will be further turned into oxygen and low-state I, thus, forming oxygen vacancies on the surface [30]. Adsorbed oxygen existed in the form of a Ti-OH bond. Figure 4d gives the XPS peak fitting diagram of Ti. The diffraction peaks of 458.24 eV and 463.95 eV belong to the Ti 2p$_{3/2}$ and Ti 2p$_{1/2}$ characteristic peaks of Ti, respectively. The characteristic peaks shifted due to the doping with I. Ti existed in the form of +4 valence. Figure 4e gives the XPS peak fitting diagram of Zn. The diffraction peaks of Zn at 1021.7 eV and 1044.8 eV correspond to the characteristic peaks of Zn 2p$_{2/3}$ (1021.3 eV) and Zn 2p$_{1/2}$ (1044.4 eV) [36]. Zn existed in the composite with +2 valence. However, due to the introduction of TiO$_2$, the diffraction peak was red-shifted by 0.4 eV [37]. Figure 4f gives the XPS peak fitting diagram of I. The peaks at 618.52 eV and 630.53 eV correspond to the peaks of I 3d$_{5/2}$ and I 3d$_{3/2}$ of I, respectively. It was generally believed that the characteristic peak at 618 eV corresponded to I$^-$ and the peak at 630 eV corresponded to I^{5+} [38,39]. Therefore, when I was doped into TiO$_2$, the valence state changed from -1 valence in KI to +5 valence, while the rest of the elements did not change their valence state.
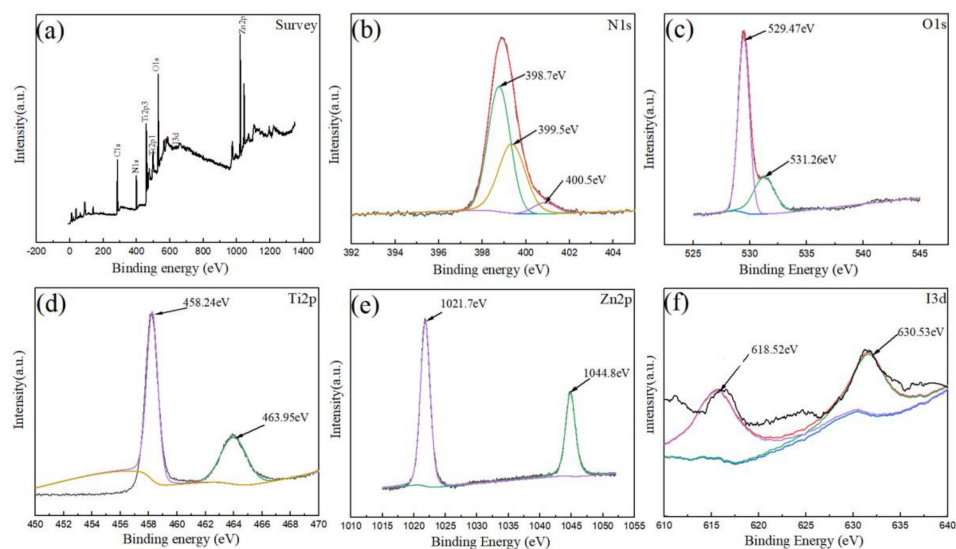
Figure 4. ZIF-8@TiO$_2$ (5%KI) XPS analysis diagram. (**a**) XPS diagram of ZIF-8@TiO$_2$ (5%KI), (**b**) XPS diagram of N element, (**c**) XPS diagram of O element, (**d**) XPS diagram of Ti element, (**e**) XPS diagram of Zn element, (**f**) XPS diagram of I element.

3.4. Analysis of Specific Surface Area

Figure 5a gives the N$_2$ adsorption desorption diagram of TiO$_2$ (5%KI). The N$_2$ adsorption–desorption curve of TiO$_2$ (5%KI) represents a type IV IUPAC curve [40]. There was a monolayer adsorption of capillary condensation. The curve appeared as a hysteresis loop and the material exhibited the capillary condensation phenomenon when the P/P_0 value was between 0.3 and 1.0. This phenomenon mostly occurs in mesoporous adsorbents. The hysteresis loop belongs to the H3 type and the adsorption amount increases with the increase in pressure. As can be seen from Table 2, the BET-specific surface area of TiO$_2$ (5%KI) is 67.233 m^2/g, the total pore volume (P/P_0 = 0.989) is 0.0976 cm^3/g, the average pore diameter is 5.8074 nm and the average pore diameter is in the range of the mesopore.
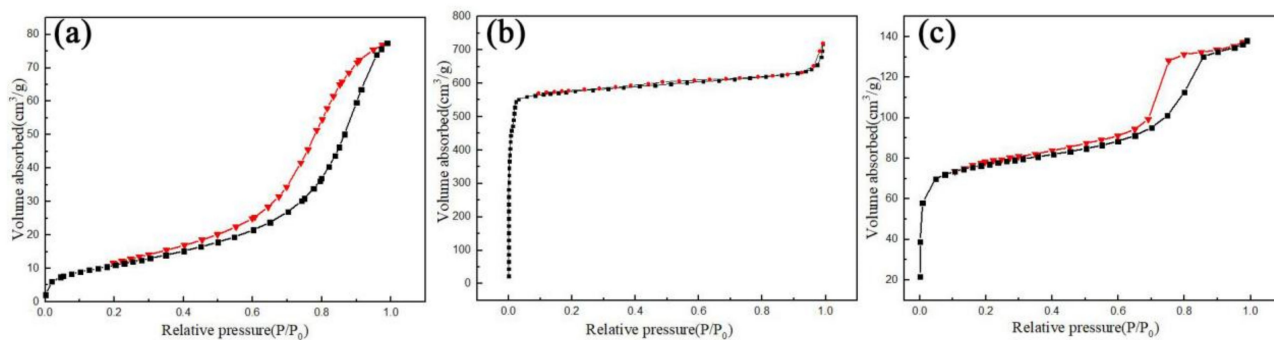

Figure 5. (**a**) N$_2$-desorption diagram of TiO$_2$ (5%KI), (**b**) N$_2$-desorption diagram of ZIF-8, (**c**) N$_2$-desorption diagram of ZIF-8@TiO$_2$ (5%KI).

Table 2. Specific surface area and pore size of TiO$_2$ (5%KI), ZIF-8, ZIF-8@TiO$_2$ (5%KI).

Sample	SBET (m^2/g)	Vpore (cm^3/g)	RAve (nm)
TiO$_2$ (5%KI)	67.233	0.0976	5.8074
ZIF-8	1853.02	1.1119	2.3243
ZIF-8@TiO$_2$ (5%KI)	289.92	0.2135	2.9461

Figure 5b gives the N$_2$ adsorption–desorption curve of ZIF-8. The N$_2$ adsorption–desorption curve of ZIF-8 represents a type I IUPAC curve, which is a microporous adsorbent with almost no hysteresis loop [40]. As can be seen from Table 2, the BET-specific

surface area of ZIF-8 is 1853.02 m^2/g, the average pore diameter is 2.3243 nm and the total pore volume ($P/P_0 = 0.9912$) is 1.1119 cm^3/g.

Figure 5c shows the N_2 adsorption–desorption curve of ZIF-8@TiO$_2$ (5%KI). The N_2 adsorption–desorption curve of ZIF-8@TiO$_2$ (5%KI) represents a type IV IUPAC curve, which is a monolayer adsorption of capillary condensation [40]. When the P/P_0 value is between 0.7 and 0.9, the hysteresis loop appears in the curve. The hysteresis loop belongs to the H2 type, which has a wide hysteresis loop and a steep desorption curve. H2-type hysteresis loops are usually found in porous materials with a wide pore diameter and various pore shapes. As can be seen from Table 2, the BET-specific surface area of ZIF-8@TiO$_2$ (5%KI) is 289.92 m^2/g, the total pore volume ($P/P_0 = 0.989$) is 0.2135 cm^3/g, the average pore diameter is 2.9461 nm and the pore type is mesopore.

It can be seen from the comparison in Figure 5a–c that the specific surface area of ZIF-8@TiO$_2$ (5%KI) is much larger than that of TiO$_2$ and much smaller than that of ZIF-8. Due to the loading of ZIF-8, the specific surface area of ZIF-8@TiO$_2$ (5%KI) is greatly improved, but is greatly reduced for ZIF-8. The ultimate goal of the experiment was to obtain a material with a higher specific surface area than TiO$_2$ through the composite of ZIF-8 and TiO$_2$. Finally, we obtained a photocatalytic material with a high specific surface area.

3.5. Analysis of UV-Vis Diffuse Reflectance Spectroscopy (UV-Vis DRS)

XRD shows that the crystal of TiO$_2$ is of the anatase type. The band gap of anatase-type TiO$_2$ was 3.2 eV when TiO$_2$ was calcined at 350 °C for 5 h. Figure 6a shows the DRS of TiO$_2$ (350 °C), TiO$_2$ (KI) and ZIF-8@TiO$_2$ (5%KI). Figure 6b provides a plot of the band gap width of the above material. The range of the light response changed, and the UV diffuse reflectance spectrum curve had a red or blue shift after the doping of KI. A red shift occurred in TiO$_2$ (5%KI), TiO$_2$ (10%KI), TiO$_2$ (15%KI) and TiO$_2$ (30%KI), which increased the light response range. The blue shift of TiO$_2$ (2%KI) and ZIF-8@TiO$_2$ (5%KI) reduced the light response range. Table 3 shows the band gap widths of samples. As can be seen from Table 3, the band gap widths of TiO$_2$ (5%KI), TiO$_2$ (10%KI), TiO$_2$ (15%KI) and TiO$_2$ (30%KI) decrease in turn, which are all smaller than the band gap of TiO$_2$ (350 °C). The reason is that the doping with I causes defects in the TiO$_2$ crystal, resulting in defective energy levels, reducing the average particle size of the crystal and increasing internal stress, which led to the overlap of electronic wave function [41]. The blue shift of TiO$_2$ (2%KI) and ZIF-8@TiO$_2$ (5%KI) was caused by the quantum size effect of the nanoparticles.
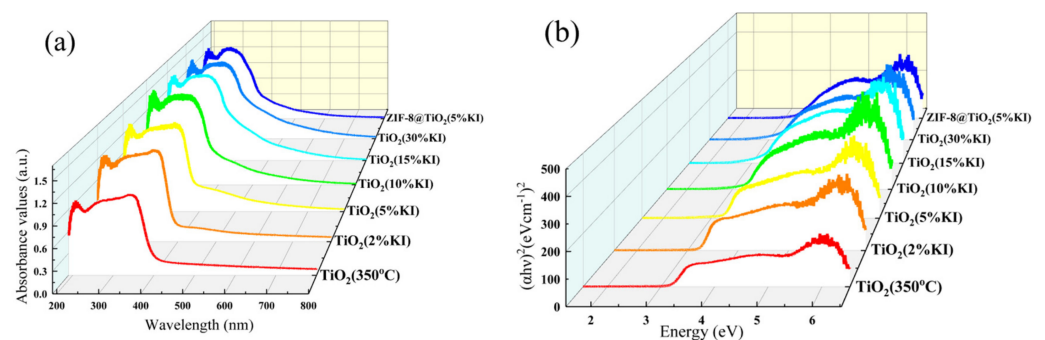

Figure 6. DRS diagram (**a**) and band gap width diagram (**b**).

Table 3. Forbidden material band widths.

Sample	TiO$_2$ (350 °C)	TiO$_2$ (2%KI)	TiO$_2$ (5%KI)	TiO$_2$ (10%KI)	TiO$_2$ (15%KI)	TiO$_2$ (30%KI)	ZIF-8@ TiO$_2$(5%KI)
Eg(eV)	3.20	3.267	3.150	3.138	2.986	2.970	3.239

3.6. Evaluation of Photocatalyst Performance

3.6.1. Effect of KI Doping Amount for Photocatalytic Efficiency

The degradation mechanism of photocatalytic materials is shown in Figure 7. The energy of UV light was greater than the band gap value of anatase TiO_2 (3.2 eV). Electrons in the TiO_2 valence band (VB) were excited to the conduction band (CB). Photogenic holes had positive potential in the valence band and photogenic electrons had negative potential in the conduction band. Photogenerated electrons combined with oxygen in the solution to form superoxide radicals (O·), and photogenerated holes combined with OH^- to form hydroxyl radicals (OH·) [42]. O· and OH· can mineralize Congo red into small molecules to achieve degradation. The doping of I atoms will generate a new valence band in the gap, which is near the valence band, due to the substitution of Ti^{4+} by I^{5+} [43], and the covalent bond features of I5s, 5P orbitals and O2p [44]. The new valence band makes it easier for photogenerated electrons to transfer to the conduction band, thus, improving the photocatalytic efficiency. ZIF-8 was coated with TiO_2, and the Congo red in the solution was adsorbed to the surface of ZIF-8. O· and OH· were transferred to the surface of ZIF-8 via the ZIF-8 channel to degrade the adsorbed Congo red.
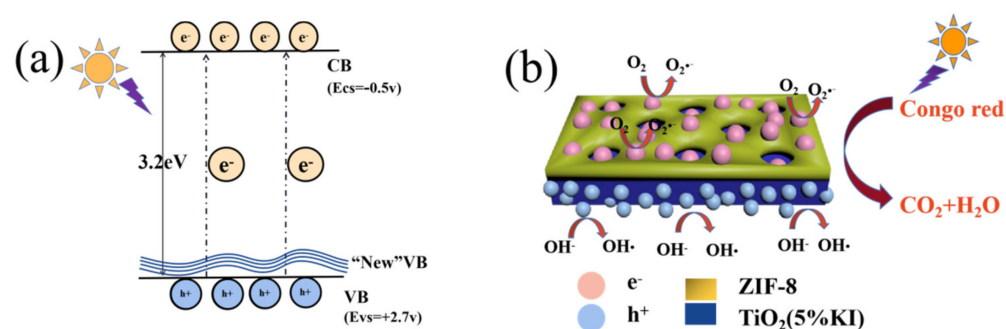

Figure 7. Schematic of the photocatalytic mechanism of (**a**) TiO_2 (KI) and (**b**) ZIF-8@TiO_2 (5%KI).

The catalysts used were TiO_2 (350 °C), TiO_2 (2%KI), TiO_2 (5%KI), TiO_2 (10%KI), TiO_2 (15%KI), TiO_2 (30%KI) and ZIF-8@TiO_2 (5%KI). The dosage of the catalyst was 20 mg. A concentration of 20 mg/L and a volume of 100 mL of Congo red solution were selected for the photodegradable material. The test process was the same as that given in 2.2.3, and the photocatalytic efficiency was calculated according to Equation (1). It can be seen from Figure 8a that the photocatalytic efficiency first increased and then decreased in TiO_2 (350 °C), TiO_2 (2%KI), TiO_2 (5%KI), TiO_2 (10%KI), TiO_2 (15%KI) and TiO_2 (30%KI). TiO_2 (5%KI) had the highest catalytic efficiency. The degradation efficiency of Congo red solution could reach 95.21% after 1 h of UV irradiation. The highest catalytic efficiency found for TiO_2 (5%KI) was due to the following reasons: The doping of I causes lattice distortion and produces a Ti-O-I bond in TiO_2 [35]. The I atoms replace Ti atoms to generate a shallow potential trap, which inhibits the recombination of the photo-generated electron and hole [45]. Therefore, the photo-generated electron and hole are further separated, and the photocatalytic efficiency is improved [46]. The light response range of TiO_2 increased and the phenomenon of red shift occurred after the doping of KI, which improved the utilization rate of ultraviolet light [47].

The doping of I into TiO_2 results in a reduction in crystal size. With different molar ratios of I doping, the crystallite size of TiO_2 (5%KI) was the smallest, reaching 14.58 nm. TiO_2 semiconductors smaller than 16 nm produced quantum size effects [48]. The valence band and conduction band in TiO_2 became relatively independent of energy levels, the valence band became more corrected, and the conduction band became more negative, which caused the oxidation and reduction ability to become stronger and the photocatalytic efficiency to improve [49]. I^{5+} ions replaced Ti^{4+} ions, which resulted in lattice distortion and a dipole moment [50]. The dipole moment had a positive effect on photoelectron-hole separation. The doping with I not only caused lattice distortion, but also caused the change in the TiO_2 band gap. The band gap became smaller. The separation of photogenerated electrons

and holes became easier, which improved the photocatalytic efficiency with KI doping. Therefore, the photocatalytic efficiency of TiO_2 can be enhanced by doping KI in TiO_2. However, with the increase in the KI doping amount, lattice distortion was caused and the crystal structure of TiO_2 was destroyed. The number of photogenerated electron-hole pairs produced by TiO_2 was greatly reduced, which reduced the photocatalytic efficiency. Excessive I doping caused the TiO_2 to generate an excessive shallow potential capture center, which increased the recombination rate of photoinduced electron-hole pairs and reduced the photocatalytic efficiency [51].
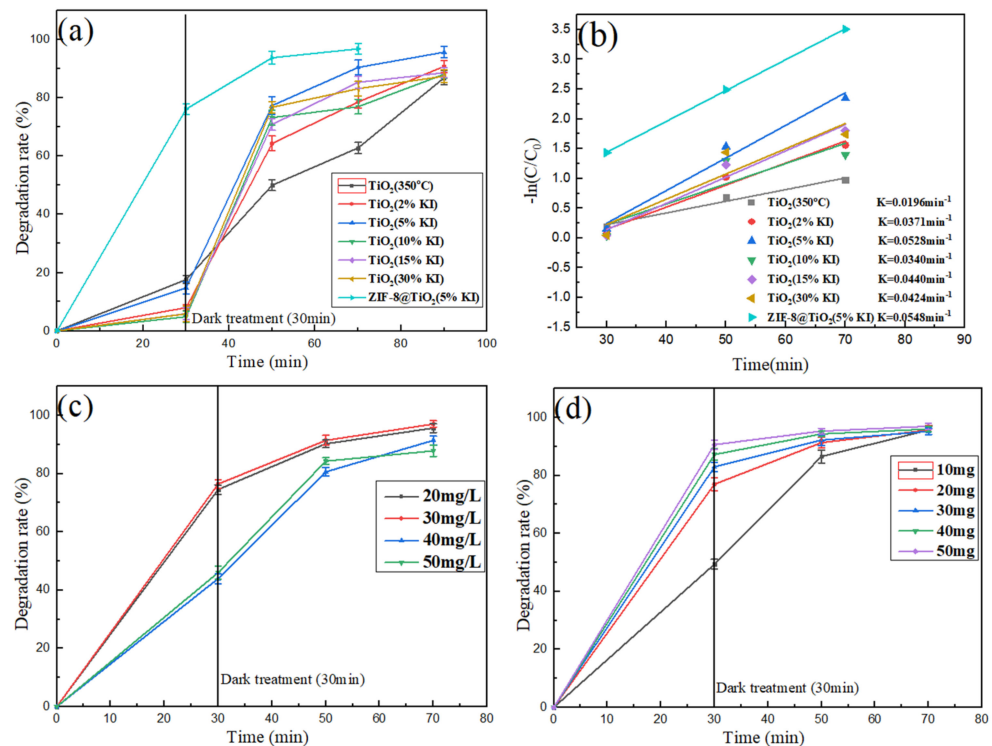

Figure 8. (**a**) ZIF-8@TiO_2 (5%KI), TiO_2 (KI) and TiO_2 (350 °C) photocatalytic efficiency diagram, (**b**) kinetic equation of Congo red degradation, (**c**) effect of the initial concentration of Congo red on catalytic efficiency, and (**d**) effect of catalyst dosage on catalytic efficiency.

The photocatalytic conditions of ZIF-8@TiO_2 (5%KI) were the same as those of TiO_2 (5%KI). However, the catalytic efficiency of ZIF-8@TiO_2 (5%KI) was higher than that of TiO_2 (5%KI), and the photocatalytic efficiency of ZIF-8@TiO_2 (5%KI) was 97% under UV irradiation for 40 min. TiO_2 (5%KI) combined with ZIF-8 greatly improved the catalytic efficiency of TiO_2 (5%KI), the main reason being that the combination of TiO_2 (5%KI) and ZIF-8 increased the specific surface area of the material. ZIF-8 provided a large number of reaction sites for the photocatalytic reaction, which solved the problem of insufficient reaction sites for TiO_2 (5%KI) and improved the photocatalytic efficiency [52].

Figure 8b shows the kinetic equation of Congo red degradation by different catalysts, which conforms to the first-order kinetic equation. The crystallite size is shown in Table 1. The kinetic equation of each material is as follows: TiO_2 (350 °C) is $-ln(C/C_0) = 0.0196x - 0.363$, TiO_2 (2%KI) is $-ln(C/C_0) = 0.0371x - 0.962$, TiO_2 (5%KI) is $-ln(C/C_0) = 0.0528x - 1.393$, TiO_2 (10%KI) is $-ln(C/C_0) = 0.034x - 0.7897$, TiO_2 (15%KI) is $-ln(C/C_0) = 0.044x - 1.179$, TiO_2 (30%KI) is $-ln(C/C_0) = 0.0424x - 1.042$, and ZIF-8@$TiO_2$ (5%KI) is $-ln(C/C_0) = 0.0548x - 0.1137$. It can be seen that the degradation rate constant of TiO_2 (5%KI) reached 0.0528 min^{-1}, and the maximum degradation rate constant of ZIF-8@TiO_2 (5%KI) reached 0.0548 min^{-1}. These results indicate that the degradation effect of the two materials on Congo red is relatively excellent.

3.6.2. Effect of Congo Red Concentration on Photocatalytic Efficiency

The dosage of the catalyst was 20 mg, the concentration of Congo red solution was 20 mg/L, 30 mg/L, 40 mg/L, and 50 mg/L and the solution volume was 100 mL. Figure 8c shows the effect of the initial concentration of Congo red solution on the catalytic efficiency. The catalytic efficiency first increased and then decreased with the increase in solution concentration. The Congo red solution of 30 mg/L had the highest catalytic efficiency. The low concentration of Congo red solution was insufficient to make full use of the reaction site. The reaction sites were fully utilized, which enhanced the photocatalytic efficiency when the concentration of Congo red solution reached 30 mg/L. The light penetration ability decreased, which resulted in a weak light response when the concentration of the solution increased. This reduced the generation rate of photogenerated carriers and the photocatalytic efficiency.

3.6.3. Effect of Dosage of ZIF-8@TiO$_2$ (5%KI) on Photocatalytic Efficiency

The catalyst was ZIF-8@TiO$_2$ (5%KI). The dosage of the catalyst was 10 mg, 20 mg, 30 mg, 40 mg and 50 mg. The concentration of Congo red solution was 30 mg/L, and the solution volume was 100 mL. The test process was the same as that in 2.2.3 and the photocatalytic efficiency could be calculated according to Equation (1). Figure 8d shows the influence of the amount of catalyst on the catalytic efficiency. The amount of catalyst was positively correlated with photocatalytic efficiency. The reaction sites and photocarriers of the catalyst increased with the increase in the amount of catalyst. Under the same conditions, the composite material produced more superoxide radicals and hydroxyl radicals to participate in the photocatalytic reaction [53].

3.6.4. Reuse

The catalyst was ZIF-8@TiO$_2$ (5%KI). The dosage of the catalyst was 20 mg. The concentration of the Congo red solution was 30 mg/L and the solution volume was 100 mL. The degradation efficiency of ZIF-8@TiO$_2$ (5%KI) was very high after 30 min of dark reaction, as shown in Figure 8a,c,d. In order to balance the adsorption reaction and photocatalytic reaction of the material and avoid the dominance of one of them in the early stages, the dark reaction was selected for 15 min and the photocatalytic reaction for 45 min. The mercury lamp was turned on and reacted for 45 min after the dark reaction for 15 min. After the reaction, 5 mL of the supernatant was centrifuged at a rotating speed of 8000 rpm to measure the absorbance A. The photocatalytic efficiency was calculated according to Equation (1). The bottom photocatalyst was collected, dried at 100 °C for 2 h and reused. As can be seen from Figure S2 (in the Supplementary Materials), the catalytic efficiency reached 83.41% after the third use and decreased to 76.42% after the fourth use. The effect was better after four cycles [54]. The reason for the decrease in catalytic efficiency was that some of the intermediate products were attached to the catalysts, which occupied the reaction site. It may have also been caused by the loss of catalysts during the processes of centrifugation, washing and drying, which led to the reduction in catalytic efficiency. The former was the dominant factor. The combination of KI and ZIF-8 improved the photocatalytic performance of TiO$_2$, which was higher than that of the same type ZIF-8@TiO$_2$ photocatalyst [21,55–57] and higher than that of the same type of Congo red degradation materials [58–63]. As shown in Table 4, the degradation effect of ZIF-8@TiO$_2$ (5%KI) showed excellent performance in the same type of materials. Compared with materials of the same type, organic pollutants can be rapidly degraded in a short time. The degradation efficiency of ZIF-8@TiO$_2$ (5%KI) was the highest in the shortest time, showing a better performance compared with other materials.

Table 4. Comparison of photocatalytic properties.

Materials	Concentration	Time (min)	Degradation of Material	Degradation Rate	Ref.
ZIF-8@TiO$_2$ (5%KI) (This work)	20 mg/L	40	Congo red	97%	This work
ZIF-8@TiO$_2$	-	120	Methylene blue	87.5%	[21]
ZIF-8@TiO$_2$	100 mg/L	120	Tetracycline	95%	[55]
ZIF-8@TiO$_2$	20 mg/L	180	Methylene blue	99%	[56]
ZIF-8@TiO$_2$	5 mg/L	40	Methylene blue	91.2%	[57]
Graphene oxide	10 mg/L	90	Congo red	85%	[58]
ZnO/SnO$_2$	5 mg/L	120	Congo red	88.14%	[59]
Graphene based Cr substituted β ZnS	20 mg/L	180	Congo red	84.49%	[60]
Silica@ZnO	20 ppm	140	Congo red	93%	[61]
Cr–ZnO	20 mg/L	60	Congo red	94%	[62]
Bi$_2$S$_3$	35 mg/L	150	Congo red	98%	[63]

4. Conclusions

In this paper, TiO$_2$ (KI) was prepared by the sol-gel method, and ZIF-8@TiO$_2$ (5%KI) was prepared by the solvothermal synthesis method. When calcined at 350 °C for 5 h, the crystal produced (KI) was anatase-type TiO$_2$. The doping with I caused the decrease in crystallite size. The ZIF-8@TiO$_2$ (5%KI) microstructure was that of an agglomeration of ZIF-8-coated TiO$_2$ (5%KI) and a part of TiO$_2$ (5%KI). The composite of ZIF-8 and TiO$_2$ (5%KI) increased the specific surface area of TiO$_2$ (5%KI). I partially replaced Ti and existed in the form of Ti-O-I in TiO$_2$ (KI). The doping with I increased the photoresponse range of TiO$_2$ and improved the efficiency of the TiO$_2$ catalysis of Congo red under ultraviolet light. TiO$_2$ (5%KI) had the highest photocatalytic efficiency. Under UV irradiation, the degradation rate of 20 mg/L and 100 mL Congo red solution by 20 mg TiO$_2$ (5%KI) for 1 h was 95.21%. Under UV irradiation, the degradation rate of 20 mg/L and 100 mL Congo red solution by 20 mg ZIF-8@TiO$_2$ (5%KI) for 40 min was 97%. The optimal concentration of Congo red solution was 30 mg/L, and the catalytic efficiency was 76.42% after being recycled four times.

Author Contributions: Conceptualization, X.Z. (Xiaotao Zhang); Investigation, Z.L. and X.Z. (Xilong Zhao); Methodology, Z.L. and W.Z.; Writing—original draft, Z.L. and W.Z.; Data curation, W.Z. and X.S.; Resources, X.Z. (Xilong Zhao); Writing—review & editing, X.Z. (Xilong Zhao), Z.C., S.W. and X.W.; Software, Z.H.; Visualization, Q.W.; Validation, Z.C.; Funding acquisition, X.Z. (Xiaotao Zhang); Supervision, X.Z. (Xiaotao Zhang) and X.W.; Project administration, X.W. All authors have read and agreed to the published version of the manuscript.

Institutional Review Board Statement: Not applicable.

Informed Consent Statement: Not applicable.

Data Availability Statement: Data sharing not applicable.

Conflicts of Interest: The authors declare no conflict of interest.

References

1. Gupta, V.K.; Suhas. Application of low-cost adsorbents for dye removal—A review. *J. Environ. Manag.* **2009**, *90*, 2313–2342. [CrossRef] [PubMed]
2. Slama, H.B.; Bouket, A.C.; Pourhassan, Z.; Alenezi, F.N.; Silini, A.; Silini, H.C.; Oszako, T.; Luptakova, L.; Golinska, P.; Belbahri, L. Diversity of synthetic dyes from textile industries, discharge impacts and treatment methods. *Appl. Sci.* **2021**, *11*, 6255. [CrossRef]
3. Rai, H.S.; Bhattacharyya, M.S.; Singh, J.; Bansal, T.K.; Vats, P.; Banerjee, U.C. Removal of Dyes from the Effluent of Textile and Dyestuff Manufacturing Industry: A Review of Emerging Techniques with Reference to Biological Treatment. *Crit. Rev. Environ. Sci. Technol.* **2005**, *35*, 19–238. [CrossRef]
4. Islam, M.A.; Ali, I.; Karim, S.M.A.; Firoz, M.S.H.; Chowdhury, A.N.; Morton, D.W.; Angovea, M.J. Removal of dye from polluted water using novel nano manganese oxide-based materials. *J. Water Process Eng.* **2019**, *32*, 100911. [CrossRef]
5. Rafii, F.; Hall, J.D.; Cerniglia, C.E. Mutagenicity of azo dyes used in foods, drugs and cosmetics before and after reduction by Clostridium species from the human intestinal tract. *Food. Chem. Toxicol.* **1997**, *35*, 897–901. [CrossRef]
6. Chung, K.T. Azo dyes and human health: A review. *J. Environ. Sci. Health Part C* **2016**, *34*, 233–261. [CrossRef]
7. Sharma, G.; Algarni, T.S.; Kumar, P.S.; Bhogal, S.; Kumar, A.; Sharma, S.; Naushad, M.; Alothman, A.Z.; Stadler, F.J. Utilization of Ag_2O–Al_2O_3–ZrO_2 decorated onto rGO as adsorbent for the removal of Congo red from aqueous solution. *Environ. Res.* **2021**, *197*, 111179. [CrossRef]
8. Zhao, D.; Wu, X.; Guan, H.; Han, E. Study on supercritical hydrothermal synthesis of $CoFe_2O_4$ nanoparticles. *J. Supercrit. Fluids* **2007**, *42*, 226–233. [CrossRef]
9. Magdalane, C.M.; Priyadharsini, G.M.A.; Kaviyarasu, K.; Jothi, A.I.; Simiyon, G.G. Synthesis and characterization of TiO_2 doped cobalt ferrite nanoparticles via microwave method: Investigation of photocatalytic performance of congo red degradation dye. *Surf. Interfaces* **2021**, *25*, 101296. [CrossRef]
10. Baruah, M.; Ezung, S.L.; Supong, A.; Bhomick, P.C.; Kumar, S.; Sinha, D. Synthesis, characterization of novel Fe-doped TiO_2 activated carbon nanocomposite towards photocatalytic degradation of Congo red. *J. Chem. Eng.* **2021**, *38*, 1277–1290. [CrossRef]
11. Kadam, A.N.; Dhabbe, R.S.; Kokate, M.R.; Gaikwad, Y.B.; Garadkar, K.M. Preparation of N doped TiO_2 via microwave-assisted method and its photocatalytic activity for degradation of Malathion. Spectrochim. *Acta Part A Mol. Biomol. Spectrosc.* **2014**, *133*, 669–676. [CrossRef] [PubMed]
12. Tojo, S.; Tachikawa, T.; Fujitsuka, M.; Majima, T. Iodine-doped TiO_2 photocatalysts: Correlation between band structure and mechanism. *J. Phys. Chem. C* **2008**, *112*, 14948–14954. [CrossRef]
13. Hui, G.H.; Wu, L.L.; Pan, M.; Chen, Y.Q.; Li, T.; Zhang, X.B. Carbon nanotube gas sensor based on corona discharge. *Chin. J. Anal. Chem.* **2006**, *34*, 1813–1816. [CrossRef]
14. Chen, B.; Eddaoudi, M.; Hyde, S.T.; O'Keeffe, M.; Yaghi, O.M. Interwoven metal-organic framework on a periodic minimal surface with extra-large pores. *Science* **2001**, *291*, 1021–1023. [CrossRef]
15. Park, K.S.; Zheng, N.; Côté, A.P.; Choi, J.Y.; Huang, R.; Uribe-Romo, F.J.; Chae, K.K.; O'Keeffe, M.; Yaghi, O.M. Exceptional chemical and thermal stability of zeolitic imidazolate frameworks. *Proc. Natl. Acad. Sci. USA* **2006**, *103*, 10186–10191. [CrossRef] [PubMed]
16. Kong, Z.C.; Liao, J.F.; Dong, Y.J.; Xu, Y.F.; Chen, H.Y.; Kuang, D.B.; Su, C.Y. Core@shell $CsPbBr_3$@zeolitic imidazolate framework nanocomposite for efficient photocatalytic CO_2 reduction. *ACS Energy Lett.* **2018**, *3*, 2656–2662. [CrossRef]
17. Zeng, X.; Huang, L.Q.; Wang, C.N.; Wang, J.S.; Li, J.T.; Luo, X.T. Sonocrystallization of ZIF-8 on electrostatic spinning TiO_2 nanofibers surface with enhanced photocatalysis property through synergistic effect. *ACS Appl. Mater. Interfaces* **2016**, *8*, 20274–20282. [CrossRef] [PubMed]
18. Liu, Q.; Zhou, B.B.; Xu, M.; Mao, G.B. Integration of nanosized ZIF-8 particles onto mesoporous TiO_2 nanobeads for enhanced photocatalytic activity. *RSC Adv.* **2017**, *7*, 8004–8010. [CrossRef]
19. Huang, Z.F.; Dong, P.M.; Zhang, Y.G.; Nie, X.X.; Wang, X.Y.; Zhang, X.W. A ZIF-8 decorated TiO_2 grid-like film with high CO_2 adsorption for CO_2 photoreduction. *J. CO_2 Util.* **2018**, *24*, 369–375. [CrossRef]
20. Zhai, L.Z.; Qian, Y.H.; Wang, Y.X.; Cheng, Y.D.; Dong, J.Q.; Shing, B.P.; Zhao, D. In situ formation of micropore-rich titanium dioxide from metal-organic framework templates. *ACS Appl. Mater. Interfaces* **2018**, *10*, 36933–36940. [CrossRef] [PubMed]
21. Chandra, R.; Mukhopadhyay, S.; Nath, M. TiO_2@ZIF-8: A novel approach of modifying micro-environment for enhanced photocatalytic dye degradation and high usability of TiO_2 nanoparticles. *Mater. Lett.* **2016**, *164*, 571–574. [CrossRef]
22. Hu, X.T.; Zhang, D.Y.; Zhao, S.Q.; Asuha, S. Hydrothermal Synthesis of Highly Water-dispersible Anatase Nanoparticles with Large Specific Surface Area and Their Adsorptive Properties. *MATEC Web Conf.* **2016**, *67*, 02013. [CrossRef]
23. Guo, H.X.; Chen, J.H.; Weng, W.; Zheng, Z.S.; Wang, D.F. Adsorption behavior of Congo red from aqueous solution on La_2O_3-doped TiO_2 nanotubes. *J. Ind. Eng. Chem.* **2014**, *20*, 3081–3088. [CrossRef]
24. Bhagwat, U.O.; Wu, J.J.; Asiri, A.M.; Anandan, S. Sonochemical Synthesis of Mg-TiO_2 nanoparticles for persistent Congo red dye degradation. *J. Photochem. Photobiol. A* **2017**, *346*, 559–569. [CrossRef]
25. Devi, L.G.; Kumar, S.G. Exploring the critical dependence of adsorption of various dyes on the degradation rate using Ln^{3+}-TiO_2 surface under UV/solar light. *Appl. Surf. Sci.* **2012**, *261*, 137–146. [CrossRef]
26. Wang, Y.Z.; Xue, X.X.; Yang, H. Preparation and characterization of carbon or/and boron-doped titania nano-materials with antibacterial activity. *Ceram. Int.* **2014**, *40*, 12533–12537. [CrossRef]

27. Mahadik, S.A.; Yadav, H.M.; Mahadik, S.S. Surface properties of chlorophyll-a sensitized TiO₂ nanorods for dye-sensitized solar cells applications. *Colloid Interface Sci. Commun.* **2022**, *46*, 100558. [CrossRef]

28. Zhang, Q.L.; Cheng, Y.L.; Fang, C.Q.; Shi, J.Y.; Chen, J.; Han, H.Z. Novel and multifunctional adsorbent fabricated by Zeolitic imidazolate framworks-8 and waste cigarette filters for wastewater treatment: Effective adsorption and photocatalysis. *J. Solid State Chem.* **2021**, *299*, 122190. [CrossRef]

29. Küsgens, P.; Rose, M.; Senkovska, I.; Fröde, H.; Henschel, A.; Siegle, S.; Kaskel, S. Characterization of metal-organic frameworks by water adsorption. *Microporous Mesoporous Mater.* **2009**, *120*, 325–330. [CrossRef]

30. Hong, X.T.; Wang, Z.P.; Cai, W.M.; Lu, F.; Zhang, J.; Yang, Y.Z.; Ma, N.; Liu, Y.J. Visible-light-activated nanoparticle photocatalyst of iodine-doped titanium dioxide. *Chem. Mater.* **2005**, *17*, 1548–1552. [CrossRef]

31. Hou, J.H.; Cao, C.B.; Idrees, F.; Ma, X. Hierarchical Porous Nitrogen-Doped Carbon Nanosheets Derived from Silk for Ultrahigh-Capacity Battery Anodes and Supercapacitors. *ACS Nano* **2015**, *9*, 2556–2564. [CrossRef] [PubMed]

32. Hulicova-Jurcakova, D.; Seredych, M.; Gao, Q.L.; Bandosz, T.J. Combined Effect of Nitrogen- and Oxygen-Containing Functional Groups of Microporous Activated Carbon on its Electrochemical Performance in Supercapacitors. *Adv. Funct. Mater.* **2009**, *19*, 438–447. [CrossRef]

33. Sun, F.G.; Wang, J.T.; Chen, H.C.; Li, W.C.; Qiao, W.M.; Long, D.H.; Ling, L.C. High Efficiency Immobilization of Sulfur on Nitrogen-Enriched Mesoporous Carbons for Li–S Batteries. *ACS Appl. Mater. Interfaces* **2013**, *5*, 5630–5638. [CrossRef] [PubMed]

34. Ishikawa, A.; Takata, T.; Kondo, J.N.; Hara, M.; Kobayashi, H.; Domen, K. Oxysulfide Sm₂Ti₂S₂O₅ as a stable photocatalyst for water oxidation and reduction under visible light irradiation (λ ≤ 650 nm). *J. Am. Chem. Soc.* **2002**, *124*, 13547–13553. [CrossRef]

35. Liu, G.; Sun, C.H.; Yan, X.X.; Cheng, L.N.; Chen, Z.G.; Wang, X.W.; Wang, L.Z.; Smith, S.C.; Gao, Q.L.; Cheng, H.M. Iodine doped anatase TiO₂ photocatalyst with ultra-long visible light response: Correlation between geometric/electronic structures and mechanisms. *J. Mater. Chem.* **2009**, *19*, 2822–2829. [CrossRef]

36. Hu, C.C.; Huang, Y.C.; Chang, A.L.; Nomura, M. Amine functionalized ZIF-8 as a visible-light-driven photocatalyst for Cr (VI) reduction. *J. Colloid Interfaces Sci.* **2019**, *553*, 372–381. [CrossRef]

37. Biesinger, M.C.; Payne, B.P.; Grosvenor, A.P.; Lau, L.W.M.; Gerson, A.R.; Smart, R.S.C. Resolving surface chemical states in XPS analysis of first row transition metals, oxides and hydroxides: Cr, Mn, Fe, Co and Ni. *Appl. Surf. Sci.* **2011**, *257*, 2717–2730. [CrossRef]

38. Usseglio, S.; Damin, A.; Scarano, D.; Bordiga, S.; Zecchina, A.; Lamberti, C. (I₂)n encapsulation inside TiO₂: A way to tune photoactivity in the visible region. *J. Am. Chem. Soc.* **2007**, *129*, 2822–2828. [CrossRef]

39. Wang, J.X.; Peng, C.R.; Chen, Z.P.; Sun, S.D.; Shi, Z.Q.; Jin, L.Q.; Zhao, W.F.; Zhao, C.S. Engineering antimicrobial and biocompatible electrospun PLGA fibrous membranes by irradiation grafting polyvinylpyrrolidone and periodate. *Colloids Surf. B* **2019**, *181*, 918–926. [CrossRef]

40. Milićević, B.; Dordević, V.; Lončarević, D.; Ahrenkiel, S.P.; Dramićanin, M.D.; Nedeljković, J.M. Visible light absorption of surface modified TiO₂ powders with bidentate benzene derivatives. *Microporous Mesoporous Mater.* **2015**, *217*, 184–189. [CrossRef]

41. Long, M.C.; Cai, W.M.; Wang, Z.P.; Liu, G.Z. Correlation of electronic structures and crystal structures with photocatalytic properties of undoped, N-doped and I-doped TiO₂. *Chem. Phys. Lett.* **2006**, *420*, 71–76. [CrossRef]

42. Sibu, C.P.; Kumar, S.R.; Mukundan, P.; Warrier, K.G.K. Structural Modifications and Associated Properties of Lanthanum Oxide Doped Sol−Gel Nanosized Titanium Oxide. *Chem. Mater.* **2002**, *14*, 2876–2881. [CrossRef]

43. Hwang, J.; Kalanur, S.S.; Seo, H. Identification of Visible Photocatalytic and Photoelectrochemical Properties of I-TiO₂ via Electronic Band Structure. *Electrochim. Acta* **2017**, *252*, 482–489. [CrossRef]

44. Niu, M.; Zhang, J.; Cao, D.P. I, N-Codoping Modification of TiO₂ for Enhanced Photoelectrochemical H₂O Splitting in Visible-Light Region. *J. Phys. Chem. C* **2017**, *121*, 26202–26208. [CrossRef]

45. Zhang, Q.Y.; Li, Y.; Ackerman, E.A.; Gajdardziska-Josifovska, M.; Li, H.L. Visible light responsive iodine-doped TiO₂ for photocatalytic reduction of CO₂ to fuels. *Appl. Catal. A Gen.* **2011**, *400*, 195–202. [CrossRef]

46. Misra, M.; Chowdhury, S.R.; Singh, N. TiO₂@Au@CoMn₂O₄ core-shell nanorods for photo-electrochemical and photocatalytic activity for decomposition of toxic organic compounds and photo reduction of Cr⁶⁺ ion. *J. Alloys Compd.* **2020**, *824*, 153861. [CrossRef]

47. Ma, Y.; Fu, J.W.; Tao, X.; Li, X.; Chen, J.F. Low temperature synthesis of iodine-doped TiO₂ nanocrystallites with enhanced visible-induced photocatalytic activity. *Appl. Surf. Sci.* **2011**, *257*, 5046–5051. [CrossRef]

48. Chen, J.H.; Yao, M.S.; Wang, X.L. Investigation of transition metal ion doping behaviors on TiO₂ nanoparticles. *J. Nanopart. Res.* **2008**, *10*, 163–171. [CrossRef]

49. Kamat, P.V. Photoelectrochemistry in particulate systems. 9. Photosensitized reduction in a colloidal titania system using anthracene-9-carboxylate as the sensitizer. *J. Phys. Chem.* **1989**, *93*, 859–864. [CrossRef]

50. Sato, J.; Kobayashi, H.; Inoue, Y. Photocatalytic Activity for Water Decomposition of Indates with Octahedrally Coordinated d¹⁰ Configuration. II. Roles of Geometric and Electronic Structures. *J. Phys. Chem. B* **2003**, *107*, 7970–7975. [CrossRef]

51. Wu, X.H.; Wang, S.; Guo, Y.; Xie, Z.Y.; Han, L.; Jiang, Z.H. Enhanced Energy Conversion Efficiency of La³⁺ Modified Nanoporous TiO₂ Electrode Sensitized with a Ruthenium Complex. Chinese. *J. Chem.* **2008**, *26*, 1939–1943. [CrossRef]

52. Qin, R.; Meng, F.M.; Khan, M.W.; Yu, B.; Li, H.J.; Fan, Z.H.; Gong, J.F. Fabrication and enhanced photocatalytic property of TiO₂-ZnO composite photocatalysts. *Mater. Lett.* **2019**, *240*, 84–87. [CrossRef]

53. Tang, M.L.; Ao, Y.H.; Wang, C.; Wang, P.F. Facile synthesis of dual Z-scheme g-C$_3$N$_4$/Ag$_3$PO$_4$/AgI composite photocatalysts with enhanced performance for the degradation of a typical neonicotinoid pesticide. *Appl. Catal. B Environ.* **2020**, *268*, 118395. [CrossRef]

54. Oh, J.T.; Chowdhury, S.R.; Lee, T.L.; Misra, M. Synergetic influence of Au/Cu$_2$O core-shells nanoparticle on optical, photo-electrochemical, and catalytic activities of Au/Cu$_2$O/TiO$_2$ nanocomposite. *Dye Pigments* **2019**, *160*, 936–943. [CrossRef]

55. Li, R.; Li, W.; Jin, C.; He, Q.Y.; Wang, Y.Z. Fabrication of ZIF-8@TiO$_2$ micron composite via hydrothermal method with enhanced absorption and photocatalytic activities in tetracycline degradation. *J. Alloys Compd.* **2020**, *825*, 154008. [CrossRef]

56. Fu, N.; Ren, X.C. Synthesis of Double-Shell Hollow TiO$_2$@ZIF-8 Nanoparticles with Enhanced Photocatalytic Activities. *Front. Chem.* **2020**, *8*, 578847. [CrossRef] [PubMed]

57. Zhong, W.L.; Li, C.; Liu, X.M.; Bai, X.K.; Zhang, G.S.; Lei, C.X. Liquid phase deposition of flower-like TiO$_2$ microspheres decorated by ZIF-8 nanoparticles with enhanced photocatalytic activity. *Microporous Mesoporous Mater.* **2020**, *306*, 110401. [CrossRef]

58. Sreelekshmi, P.B.; Pillai, R.R.; Meera, A.P. Controlled Synthesis of Novel Graphene Oxide Nanoparticles for the Photodegradation of Organic Dyes. *Top. Catal.* **2022**, 1–10. [CrossRef]

59. Sayadi, M.H.; Ghollasimood, S.; Ahmadpour, N.; Homaeigohar, S. Biosynthesis of the ZnO/SnO$_2$ nanoparticles and characterization of their photocatalytic potential for removal of organic water pollutants. *J. Photochem. Photobiol. A* **2022**, *425*, 113662. [CrossRef]

60. Dake, D.V.; Raskar, N.D.; Mane, V.A.; Sonpir, R.B.; Khawal, H.A.; Deshpande, U.; Stathatos, E.; Dole, B.N. Photocatalytic performance of graphene-based Cr-substituted β ZnS nanocomposites. *Appl. Phys. A* **2022**, *128*, 276. [CrossRef]

61. Afsharpour, M.; Amoee, S. Porous biomorphic silica@ZnO nanohybrids as the effective photocatalysts under visible light. *Environ. Sci. Pollut. Res.* **2022**, 1–12. [CrossRef] [PubMed]

62. Elamin, N.; Modwi, A.; Aissa, M.A.; Taha, K.K.; Al-Duaij, O.K.; Yousef, T.A. Fabrication of Cr–ZnO photocatalyst by starch-assisted sol–gel method for photodegradation of congo red under visible light. *J. Mater. Sci. Mater. Electron.* **2021**, *32*, 2234–2248. [CrossRef]

63. Sambathkumar, C.; Manirathinam, V.; Manikandan, A.; Kumar, M.K.; Sudhahar, S.; Devendran, P. Solvothermal synthesis of Bi$_2$S$_3$ nanoparticles for active photocatalytic and energy storage device applications. *J. Mater. Sci. Mater. Electron.* **2021**, *32*, 20827–20843. [CrossRef]